Published by IOP Publishing for Sissa Medialab

Received: *February 3, 2026*
Revised: *April 2, 2026*
Accepted: *May 13, 2026*
Published: *June 12, 2026*

TECHNICAL REPORT

Development of a comprehensive PMT optical model for the JUNO experiment

Y. Ren[a,b] **X. Yang**[a] **Y. Wang**[c] **Z. Deng**[a,*] **Z. Qin**[a] **A. Olshevskiy**[d] **W. Wang**[e,f] **N. Anfimov**[d] **Z. Wang**[a] **and G. Cao**[a,b]

[a] *Institute of High Energy Physics, Chinese Academy of Sciences, Beijing 100049, China*
[b] *University of Chinese Academy of Sciences, Beijing 100049, China*
[c] *Shandong University, Jinan 250100, China*
[d] *Joint Institute for Nuclear Research, Dubna, Moscow Region 141980, Russia*
[e] *Sino-French Institute of Nuclear Engineering and Technology, Sun Yat-sen University, Zhuhai 519082, China*
[f] *School of Physics, Sun Yat-sen University, Guangzhou 510275, China*

E-mail: dengzy@ihep.ac.cn

Abstract: Developing a precise optical model for the photomultiplier tubes (PMTs) is crucial for enhancing the accuracy of detector simulations and refining the energy response model at the Jiangmen Underground Neutrino Observatory (JUNO), where 17,596 20-inch PMTs were installed. In this study, we established a comprehensive PMT optical model based on the prior studies, taking into account the non-uniformity of the photon detection efficiency (PDE) across the PMT surface and variations in PDE as well as reflectance among different PMTs. By collecting the reflectance data from 669 PMTs and utilizing the PDE data from mass testing systems, we estimated thickness maps of the photocathode (PC) and the anti-reflective coating (ARC) for each PMT. We also determined the collection efficiency (CE) by decomposing PDE with consideration of the optical processes occurring within PMTs. The refractive index and extinction coefficient of both the PC and ARC, along with the escape factor, were evaluated over a broad wavelength range of 300 nm to 700 nm, covering the entire spectrum of interest for JUNO. Compared to the prediction from a simplified PMT optical model, which assumes the uniform PC and ARC across all PMTs of the same type, the further developed PMT optical model yields much more reflectance for HPK PMTs and less for NNVT PMTs, and the change in PDE is at the level of a few percent. This comprehensive PMT optical model also provides a valuable reference for other PMT-based applications.

Keywords: Detector modelling and simulations I (interaction of radiation with matter, interaction of photons with matter, interaction of hadrons with matter, etc); Photon detectors for UV, visible and IR photons (vacuum) (photomultipliers, HPDs, others); Simulation methods and programs

ArXiv ePrint: 2601.19081

*Corresponding author.

© 2026 IOP Publishing Ltd and Sissa Medialab.
All rights, including for text and data mining, AI training, and similar technologies, are reserved.

https://doi.org/10.1088/1748-0221/21/06/T06002

Contents

1 Introduction **1**

2 A comprehensive PMT optical model **3**
2.1 A summary of the existing PMT optical model 3
2.2 Extension of the PMT optical model 4

3 PDE and reflectance data **6**
3.1 PDE data 6
3.2 Reflectance data 7

4 Results **10**
4.1 Thickness map of the PC and ARC 10
4.2 CE 10
4.3 Spectral response of optical properties 11
4.4 Comparison of the average reflectance and PDE 12

5 Conclusion **13**

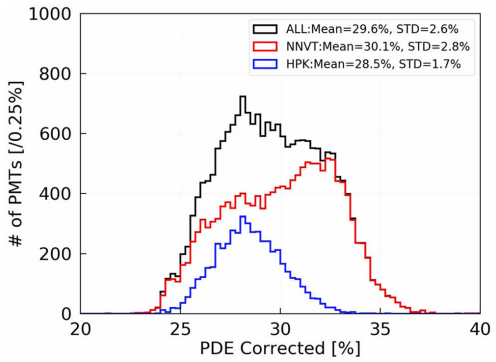
2026 JINST 21 T06002

1 Introduction

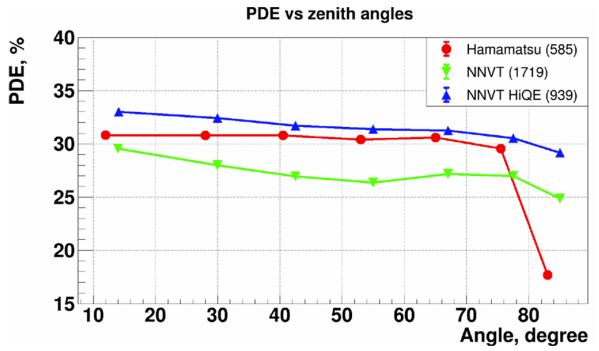
The photomultiplier tube (PMT) has served as an optimal photosensor for numerous neutrino projects [1–9] over the past few decades and remains pivotal in current and future initiatives. One such project is the Jiangmen Underground Neutrino Observatory (JUNO), which has deployed 17,596 20-inch PMTs and 25,587 3-inch PMTs in its central detector. The spherical arrangement of these PMTs achieves up to 75% photocathode (PC) coverage. Among 20-inch PMTs, 4,939 are dynode PMTs manufactured by Hamamatsu Photonics K.K. (HPK) [10], while the remainder are MCP-PMTs produced by Northern Night Vision Technology Co. (NNVT) [11]. These PMTs are responsible for capturing light from the 20 kton liquid scintillator contained within an acrylic sphere with a diameter of 35.4 m. The detailed design of the JUNO detector is described in [12]. The primary goal of JUNO is to determine the neutrino mass ordering and precisely measure neutrino oscillation parameters by analyzing oscillation patterns within the neutrino energy spectrum from Taishan and Yangjiang nuclear power plants, located approximately 53 km from the JUNO site. Additionally, JUNO has an extensive physics program focused on detecting neutrinos from various natural sources, as outlined in [13, 14]. JUNO has started physics data taking since August 2025 and published the first measurement of reactor neutrino oscillations [15], with the majority of detector performances achieving requirements [16].

A precise understanding of the detector response is crucial for determining the neutrino mass ordering and conducting other physics analyses in JUNO [18]. Specifically, the detector response primarily involves the energy resolution, energy non-uniformity, and energy non-linearity within the JUNO detector. The responses of PMTs, particularly the photon detection efficiency (PDE), significantly influence these energy responses and must be carefully managed. PDE could be decomposed into the quantum efficiency (QE) and collection efficiency (CE). QE is the product of

the photon absorption ratio in the PC and the escape factor, which represents the fraction of free photoelectrons emitted from the PC, according to Spicer's three-step model [19]. CE represents the probability of detecting the photoelectron. The factors that affect QE and CE, including the working media, the angle of incidence (AOI) of photons, photon energy, positions where the light hits the PC, and the shape as well as the internal structure of PMTs, are discussed in detail in [20]. Within the JUNO experiment, PDE of 20-inch PMTs has been thoroughly characterized via the PMT mass testing system, including the average PDE measured with the container system for all PMTs and PDE uniformity measured with the scanning station system for a subset. The container system provided the parallel light illuminating the PMT surface uniformly, and the tested PDE distributions are shown in figure 1(a). While the scanning station system was utilized to test PDE uniformity with seven LEDs at different zenith angles (θ), rotating along the azimuthal angle, and the results of average PDE curves along the zenith angle are shown in figure 1(b). However, the measured PDE cannot be directly utilized in detector simulations to predict energy responses because PMTs operate in water within the JUNO detector, rather than in air, and the AOIs, energies, and positions of photons hitting PMTs differ from those in the mass testing system. In fact, these factors can vary significantly from event to event in the JUNO detector and lead to different PDE. Therefore, a PMT optical model is essential to accommodate all these factors while adhering to constraints from mass testing data.



(a) PDE distributions measured with the container system



(b) Average PDE along the zenith angle measured with the scanning station system

Figure 1. (a) The PDE distributions measured with the container system for all PMTs (black), NNVT PMTs (red), and HPK PMTs (blue). (b) The average PDE along the zenith angle measured with the scanning station system for HPK PMTs (red), NNVT normal-QE PMTs (green), and NNVT high-QE PMTs (blue). Reproduced from [17]. CC BY 4.0.

A new optical model for PMTs has been proposed in [20], which accounts for the PMT window as a composite structure comprising the glass substrate, a thin film of anti-reflective coating (ARC), and a thin film of PC, illustrated in figure 2 with a description of light propagation. The thin films of ARC and PC form the coherent layers, which could lead to light interference. The key parameters of this model were determined from detailed measurements performed on three 20-inch PMTs: two from NNVT and one from HPK. By incorporating the optical properties of the PC and ARC extracted from these measurements into the JUNO simulation program, the energy response of the JUNO detector has been evaluated and predicted under the assumption that PMTs of the same type share the identical optical properties of the PC and ARC [21]. However, the variations in PDE exist among

2026 JINST 21 T06002

PMTs, and the properties of the PC and ARC could be non-uniform. Moreover, the PMT reflectance exhibits significant variations, which must also be taken into account, as light reflected from PMTs has a substantial impact on the light yield and energy response in the JUNO detector. In this study, these effects are incorporated by extending the PMT optical model originally developed in [20]. The extension utilizes the PDE data acquired from both the container system and scanning station system, as well as the reflectance data collected in this study. The resulting comprehensive PMT optical model enables the decoupling of QE and CE from the measured PDE, while accounting for the non-uniformity of the PC and ARC. Utilizing this model, we derived thickness maps of the PC and ARC for all 17,596 20-inch PMTs, along with their corresponding CE values. The model covers the entire ranges of photon wavelengths relevant to JUNO, from 300 nm to 700 nm. This comprehensive approach also provides valuable insights for other PMT-based projects seeking to improve their detector performance.

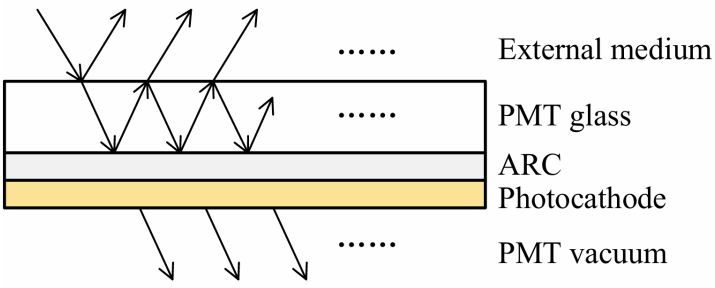


Figure 2. The structure of the PMT window and light propagation. Reproduced from [20]. CC BY 4.0.

The subsequent sections are organized as follows: we first review the PMT optical model developed in [20], followed by a detailed discussion of the comprehensive PMT optical model. We then introduce the PDE data utilized in this study, and illustrate the method employed for PMT reflectance measurements and report reflectance results. Subsequently, the extracted basic parameters for the PMT optical simulation are discussed, including thickness maps of the PC and ARC and CE for individual PMTs, as well as the refractive index and extinction coefficient over an extended wavelength range for three types of PMTs. In the end, the comparison of the average reflectance and PDE calculated from simplified and comprehensive models is presented.

2 A comprehensive PMT optical model

2.1 A summary of the existing PMT optical model

PDE could be denoted as a function of the photon wavelength (λ), the AOI (α), and the position ($\vec{r}$) of the photon hitting the PC of PMTs. Specifically, the measured PDE can be contributed by multiple positions in addition to the point of incidence on the PC, as a fraction of the incident light could penetrate the PC and propagate within PMTs. These transmitted photons could hit the PC again and then be absorbed, or even undergo multiple reflections before absorption. Consequently, PDE can be expressed as shown in eq. (2.1) and is discussed in detail in [20]:

$$\mathrm{PDE}(\lambda,\alpha,\vec{r}) = \sum_j a_j(\lambda,\alpha,\vec{r}) \cdot \beta_j(\lambda,\alpha,\vec{r}) \cdot \rho_j(\lambda) \cdot \mathrm{CE}_j(\vec{r}) = \sum_j a_j(\lambda,\alpha,\vec{r}) \cdot \beta_j(\lambda,\alpha,\vec{r}) \cdot F_j(\lambda,\vec{r}) \tag{2.1}$$

2026 JINST 21 T06002

Here, j represents the j-th photon, and a represents the absorption ratio of the incident light. The coefficient β weights the absorption from different positions that contribute to the measured PDE, and ρ is the escape factor. The a, β and ρ are decoupling from QE, and the product of ρ and CE is denoted as an F-factor. For the ideally uniform PC and ARC, the positional dependencies of a and ρ would be negligible. While this assumption may hold in certain applications, it is generally not valid for large PMTs, such as those employed in JUNO. The realistic non-uniform optical parameters of the PC and ARC could lead to the non-uniformity of the absorptance, which contributes to non-uniform PDE.

CE is determined by the electric field distribution within PMTs, which typically varies with positions on the PC, contributing to PDE non-uniformity as well. By selecting several reference positions with known F-factors on the PC, the F-factor at any other position can be derived through interpolation. Therefore, eq. (2.1) can be rewritten as:

$$\mathrm{PDE} = \sum_j a_j \sum_{k=1}^{n} \beta_{jk} F_k \tag{2.2}$$

where β represents the weight coefficient, and F_k denotes the F-factor at the k-th reference point. A procedure for deriving the F-factors at these reference points has been proposed in [20]. The coefficient β can be computed by simulating the optical processes inside PMTs utilizing a simulation toolkit. The absorptance, reflectance, and transmittance of incident photons on the PC can be calculated based on the optical theory with the optical properties of the PC and ARC, including the refractive index (n), extinction coefficient (k), and thickness (d). In the previous work, the reflectance data collected by immersing PMTs in the linear alkylbenzene are utilized to extract values for n, k, and d for two NNVT PMTs and one HPK PMT across a wavelength range of 390 nm to 500 nm. These PMTs represent three different types of 20-inch PMTs equipped in the JUNO detector. For NNVT PMTs, there are two types known as NNVT normal-QE PMT and NNVT high-QE PMT, which were produced during the early stages of the PMT mass production and manufactured with the improved QE achieved through the optimized PC technology, respectively.

2.2 Extension of the PMT optical model

The following assumptions have been made to enable the PMT optical model to account for PDE non-uniformity within a single PMT and PDE variations among different PMTs:

- PMTs of the same type share the identical spectral responses for the refractive index and extinction coefficient of both the PC and ARC. The values of n and k, as well as the escape factor, acquired in [20], are employed in this study for three types of PMTs, covering the wavelengths from 390 nm to 500 nm. Utilizing dispersion relations and available data in the literature, we extend this range down to 300 nm and up to 700 nm, encompassing the relevant spectrum for JUNO.

- The variations in QE and reflectance for a single PMT are induced by non-uniform thicknesses of the PC and ARC. The thickness map is determined in this work according to the optical theory, with inputs derived from the PDE and reflectance data for each 20-inch PMT. These inputs will be discussed in detail in section 3.

- Due to the absence of QE position-dependent data across the PMT surface, decoupling the position dependence of QE and CE from measured PDE presents some challenges. Therefore,

2026 JINST 21 T06002

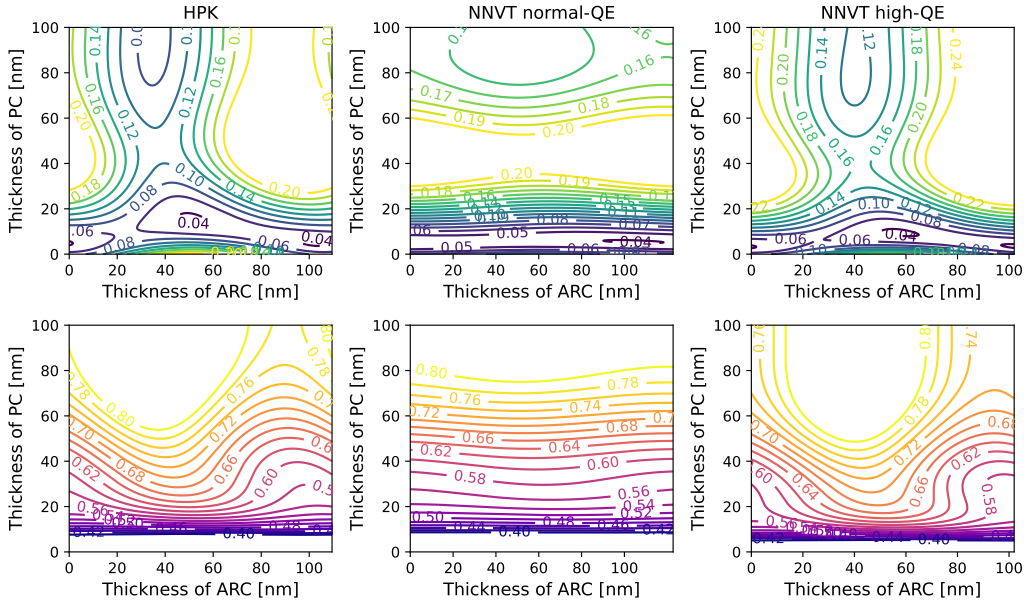


Figure 3. The contours of the reflectance (top) and absorptance (bottom) at 415 nm and 420 nm, respectively, as a function of thicknesses of the ARC (x-axis) and PC (y-axis) for HPK PMT (left), NNVT normal-QE PMT (middle) and NNVT high-QE PMT (right).

we assume that CE remains constant in the PC region for zenith angles smaller than 70 degrees (in regions far from the equator) when calculating thickness maps of the PC and ARC. Thereafter, the positional dependence of CE and its variations among different PMTs are incorporated into eq. (2.2).

- For simplification, we assume that both QE and CE are independent of azimuthal angles on the PC. This assumption is a reasonable approximation for QE of both NNVT PMTs and HPK PMTs, as demonstrated in [17]. Regarding CE, while it is azimuthal angle-dependent for HPK PMTs near the equator due to the orientation of the focusing electrode, the random arrangement of these electrodes during the PMT installation in the JUNO detector largely mitigates their impact on energy responses, as contributions from the multiple PMTs during physical events sufficiently average out these variations.

Given the assumptions above, the thickness map of the PC and ARC can be derived by simultaneously fitting the PDE from [17] and reflectance data collected in this study for all 20-inch PMTs. To model the position dependence of the thickness for both the PC and ARC, an empirical formula is employed:

$$d_{\mathrm{PC,ARC}} = c_{2_{\mathrm{PC,ARC}}} \cdot \theta^2 + c_{1_{\mathrm{PC,ARC}}} \cdot \theta + c_{0_{\mathrm{PC,ARC}}} \tag{2.3}$$

where θ represents the zenith angle of the position on the PC, while c_0, c_1, and c_2 are the free parameters determined through the fitting process. Figure 3 illustrates the contours of the reflectance (top) and absorptance (bottom) at 415 nm and 420 nm, respectively, calculated as a function of thicknesses of the ARC (x-axis) and PC (y-axis) for HPK PMT (left), NNVT normal-QE PMT (middle), and NNVT high-QE PMT (right). The refractive index and extinction coefficient of the ARC and PC

2026 JINST 21 T06002

reported in [20] are used in these calculations. Notably, different types of PMTs exhibit distinct dependencies in their thickness maps, and a value of reflectance or absorptance could be induced by multiple combinations of thicknesses of ARC and PC. Specifically, the thickness of ARC has an insignificant influence on the reflectance and absorptance for NNVT normal-QE PMT. Once thickness maps of the PC and ARC are established, the non-uniformity of the absorptance on the PC can be calculated. The weight coefficients are computed by simulating the optical processes within PMTs utilizing a simulation program developed based on Geant4 [22]. Subsequently, CE at the reference points can be determined with the PDE data at those points (the zenith angles in table 1 in the next section) via eq. (2.2), and then CE at other points can be derived by interpolation.

3 PDE and reflectance data

In this study, both the PDE results measured with mass testing systems including the container system and scanning station system and the newly collected reflectance data are utilized to constrain thicknesses of the PC and ARC.

3.1 PDE data

For each 20-inch PMT, PDE is measured with a container system that employs a 420 nm light source to illuminate the entire PMT PC in air. Additionally, a subset of PMTs is evaluated for PDE uniformity test with a scanning station system, which scans the PC with seven LEDs that provide 420 nm light nearly perpendicular to the surface at seven zenith angles, meanwhile LEDs can be rotated to cover different azimuth angles. PDE obtained from the container system is then corrected to align with PDE as defined by the scanning station system, which averages the PDE values acquired at positions of seven LEDs, weighted by their respective surface areas. Table 1 summarizes the surface area weights along with zenith angles for each LED for both NNVT and HPK PMTs. In this study, PDE values averaged over azimuthal angles for seven zenith angles are utilized to extract thickness maps of the PC and ARC.

Table 1. The zenith angles and surface area weights of seven LEDs equipped in the scanning station system.

	LED1	LED2	LED3	LED4	LED5	LED6	LED7
Zenith angle (NNVT)	14°	30°	42.5°	55°	67°	77.5°	85°
Area weight (NNVT)	4.85%	8.97%	12.58%	17.21%	19.92%	18.04%	18.43%
Zenith angle (HPK)	13°	28°	41°	55°	66°	79°	85°
Area weight (HPK)	4.51%	8.76%	13.49%	17.11%	20.46%	18.65%	17.03%

However, since only approximately 3,200 PMTs were evaluated with the scanning station system, it is necessary to develop a method to estimate the PDE values at seven zenith angles for PMTs that were not tested in this system in order to simulate their PDE non-uniformity as well. A straightforward approach to predict these PDE values is to perform random sampling based on the measured data. To account for the potential dependence of PDE on zenith angles, a seven-dimensional PDE histogram is constructed according to the data collected with the scanning station system for each type of PMT, which includes 585 HPK PMTs, 1,719 NNVT normal-QE PMTs, and 939 NNVT high-QE PMTs. The random sampling of PDE is carried out with the seven-dimensional PDE histograms, which allows the determination of

2026 JINST 21 T06002

the PDE values at seven reference positions for all PMTs that were not tested with the scanning station system. A normalization factor is applied to the seven sampled values during the sampling process to ensure that the average sampled PDE of each PMT aligns with the PDE results acquired from the container system, where the average PDE is calculated by applying the weights presented in table 1.

Since the PDE obtained above encompasses the contributions from the transmitted photons absorbed at multiple positions on the PC in addition to the direct absorption at the incident position, a detailed PMT optical simulation is conducted to distinguish the absorbed positions of photons. Utilizing the PMT optical simulation software developed in [20], the detailed structure of seven LED light sources has been newly implemented in the software, reflecting their real locations and orientations in the scanning station system, which allows for accurate accounting of the distributions of the AOI and the beam profile of light impinging on the PMT surface. The simulations for seven LEDs were conducted with the uniform optical properties of the PC and ARC acquired from [20]. Figure 4 illustrates the zenith angle distributions of the absorbed photons for seven LEDs for HPK PMT (red), NNVT normal-QE PMT (green), and NNVT high-QE PMT (blue). This figure indicates that the total absorption primarily arises from the incident positions of light beams, which are represented by the peak, while the rest shows the contributions from the transmitted photons. The ratio of the absorbed transmitted photons to the total absorbed photons is depicted in the last panel and applied to correct PDE by excluding these extra contributions based on their weights. It is observed that two types of NNVT PMTs exhibit the similar distributions due to their same shape and structure, and compared to HPK PMTs, they gain the significantly larger contributions from the transmitted photons.

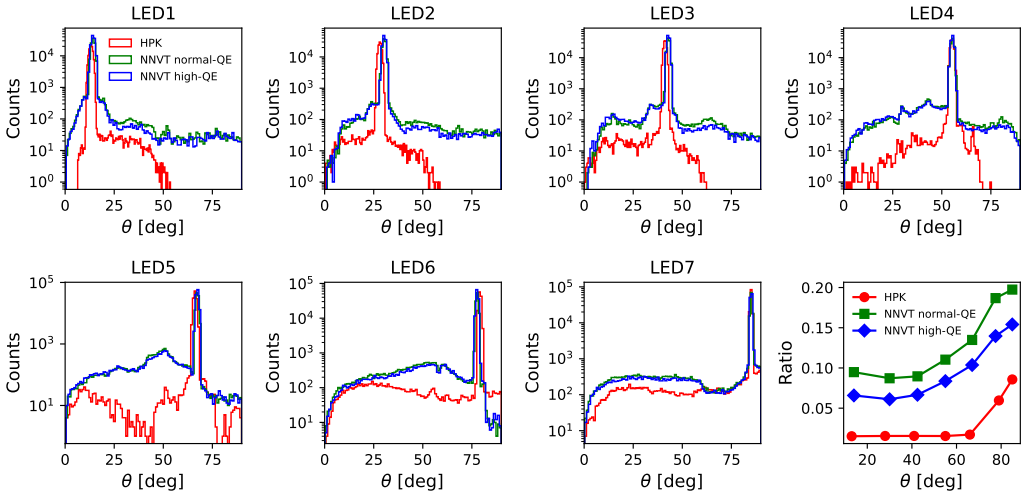


Figure 4. The zenith angle distributions of the absorbed photons for seven LEDs for HPK PMT (red), NNVT normal-QE PMT (green), and NNVT high-QE PMT (blue), and the ratio of the absorbed transmitted photons to the total absorbed photons is shown in the last panel.

3.2 Reflectance data

The reflectance measurements were carried out, utilizing the setup developed in this work. In the first stage, a total of 565 20-inch PMTs were randomly selected for testing, which included 276 HPK PMTs, 115 NNVT normal-QE PMTs, and 174 NNVT high-QE PMTs. The reflectance was

2026 JINST 21 T06002

measured at 415 nm across four different zenith angles, including 0°, 28°, 51° and 72°. In the second stage, only PMTs tested with the scanning station system were selected, and measured at four zenith angles as well as the azimuth angles scanned with a step of 45°, involving 21 HPK PMTs, 38 NNVT normal-QE PMTs, and 45 NNVT high-QE PMTs.

The schematic diagram of the reflectance measurement setup is shown in figure 5. The system consists of an LED light source coupled with an optical fiber, with a central wavelength of 415 nm and a full width at half maximum of 14 nm. An integrating sphere, the ISP-50-8-REFL from Mikropack, is employed to collect the reflected light from the tested samples, along with a spectrometer and a computer for data storage, while a testing mold provides the positional information on PMTs. In the setup, optical fiber #1 transmits the light from the LED to the integrating sphere, where the light beam is collimated by a lens integrated at the top of the sphere. The incident light beam exits the sphere at an AOI of 8° through a hole at the bottom, which has a diameter of approximately 8 mm. When a sample is placed over this hole, the reflected light is collected by the integrating sphere, and a fraction of the light is transmitted through optical fiber #2 to the spectrometer, where its intensity is measured as a function of the wavelength. The reflectance of the test sample can be determined by comparing its reflected intensity with that of the reference sample, which has been calibrated. This measurement does not require dark conditions, as the background spectrum can be directly measured without samples placed over the hole of the integrating sphere. Figure 6 illustrates an example of measured spectra: the background (blue), the PMT (green), and the reference sample (orange).

The systematic uncertainty has been carefully estimated, with the relative uncertainty determined to be approximately 2.5%. The primary contributions to the uncertainty arise from the LED stability and the reflectance uncertainty of the reference sample. Additionally, the reflectance of PMT was corrected by a ratio for each zenith angle to eliminate the influence of the curvature of the PMT surface on the reflectance. This ratio is defined as the reflectance of a reflective film measured on the flat surface to that on the curved surface which was measured by covering the PMT with the film. Since no dependence of the reflectance on the azimuthal direction was observed, the reflectance values measured at different azimuth angles are finally averaged for each zenith angle.

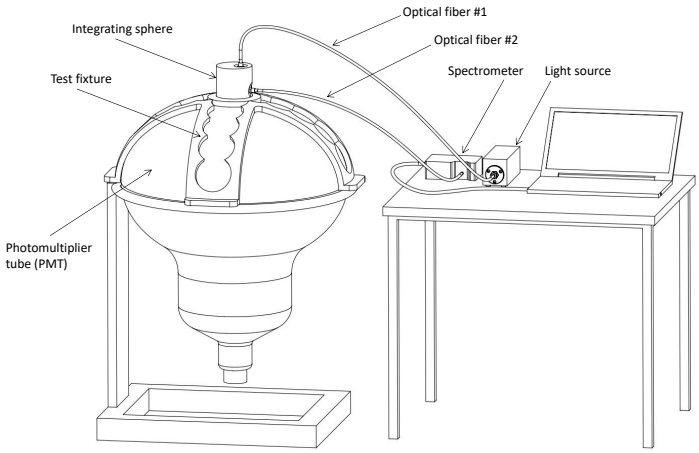


Figure 5. The schematic diagram of the reflectance setup.

2026 JINST 21 T06002

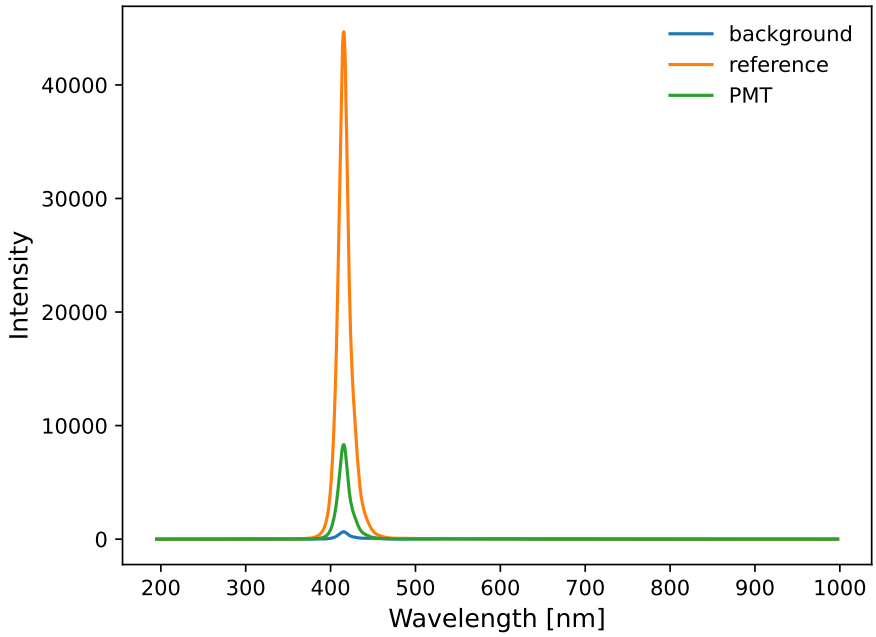


Figure 6. An example of measured spectra: the background (blue), the PMT (green), and the reference sample (orange).

The measured results are presented in figure 7, showing data for all tested HPK PMTs (left), NNVT normal-QE PMTs (middle), and NNVT high-QE PMTs (right), and the solid blue lines represent the average reflectance for each type of PMT. The significant variations in the reflectance can be observed across all types of PMTs. Specifically, the average reflectance at 0° for HPK PMTs is approximately 5.9%, which is lower than 10.8% and 16.4% observed for NNVT normal-QE and NNVT high-QE PMTs, respectively. Additionally, the reflectance of HPK PMTs increases in areas closer to the equator; in contrast, the reflectance of NNVT PMTs exhibits a decreasing trend from 0° to about 50°, followed by an increase.

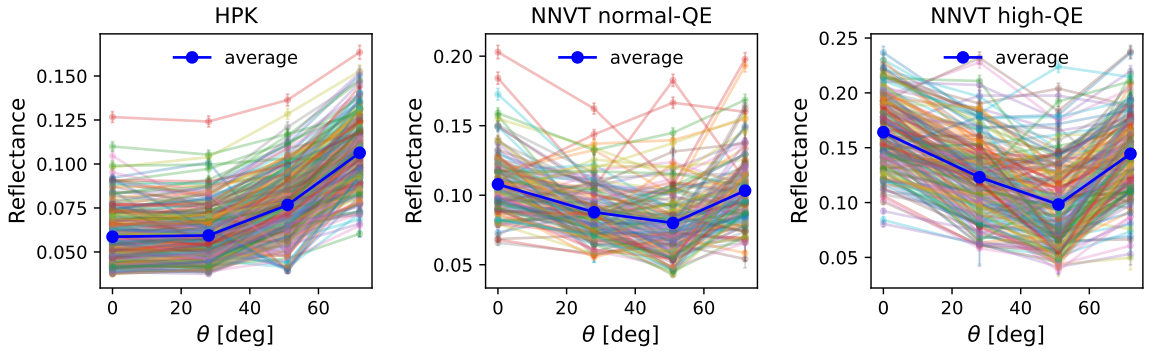


Figure 7. The measured reflectance of HPK PMTs (left), NNVT normal-QE PMTs (middle), and NNVT high-QE PMTs (right). The solid blue lines represent the average reflectance for each type of PMT.

2026 JINST 21 T06002

A similar random sampling approach to that applied for estimating PDE is employed to assess the reflectance of PMTs that have not been measured. A four-dimensional reflectance histogram is constructed with the measured data for each type of PMT to account for the positional dependence of the reflectance. Since the collected data indicate a weak correlation between the reflectance and PDE, this relationship is not considered in the aforementioned sampling process.

4 Results

4.1 Thickness map of the PC and ARC

A chi-squared function is constructed to simultaneously fit the reflectance and PDE data:

$$\begin{aligned}\chi^2 = &\sum_{i=1}^{4}\left(\frac{R(\theta_i) - R_{\text{theo}}(d_{\text{PC}}(\theta_i), d_{\text{ARC}}(\theta_i))}{\sigma_R}\right)^2 \\ &+ \sum_{j=1}^{5}\left(\frac{A(\theta_j) - A_{\text{theo}}(d_{\text{PC}}(\theta_j), d_{\text{ARC}}(\theta_j))}{\sigma_A}\right)^2 \\ &+ \left(\frac{\text{CE}' - \text{CE}_{\text{theo}}}{\sigma_{\text{CE}'}}\right)^2\end{aligned} \tag{4.1}$$

In this equation, $R(\theta_i)$ represents the measured reflectance at four zenith angles, while R_{theo} and A_{theo} are the calculated reflectance and absorptance, respectively, based on the optical theory. The predicted CE_{theo} is set to 0.93 for HPK PMTs and 1.0 for NNVT PMTs [21]. The uncertainties σ_R, σ_A, and $\sigma_{\text{CE}'}$ correspond to the measured reflectance, expected absorptance, and assumed constant CE′, respectively. Here, $\sigma_{\text{CE}'}$ is assumed to be 3%, and σ_A is estimated through error propagation, as the absorptance $A(\theta_j)$ can be calculated via:

$$A(\theta_j) = \frac{\text{PDE}'(\theta_j)}{\rho \cdot \text{CE}'} \tag{4.2}$$

where PDE′ represents the corrected PDE, which excludes the contributions from the absorbed transmitted photons to the total PDE. The uncertainty of PDE′ is assumed to be 3%, consistent with the uncertainty of PDE from the mass testing. Only the PDE measured at five small zenith angles, namely from LED1 to LED5, are utilized in the fitting process with the assumption that CE remains constant in this region. The value and uncertainty of ρ is at 420 nm from [20].

By minimizing eq. (4.1), the free parameters c_0, c_1, and c_2 in eq. (2.3) can be constrained for both the PC and ARC of each PMT. An example of the thickness curves derived from the fitting is illustrated in figure 8 for HPK PMT (left), NNVT normal-QE PMT (middle), and NNVT high-QE PMT (right). Since the thickness of the ARC has a negligible effect on the reflectance and absorptance for NNVT normal-QE PMTs, as demonstrated in figure 3, it is fixed at 49.1 nm, which is taken from [20]. The obtained thickness distributions at 0° are presented in figure 9 for all HPK PMTs (left), NNVT normal-QE PMTs (middle), and NNVT high-QE PMTs (right).

4.2 CE

The aforementioned PMT optical simulation is conducted again for seven LEDs in the scanning station system by incorporating the constructed thickness map for each PMT into the simulation. This allows

2026 JINST 21 T06002

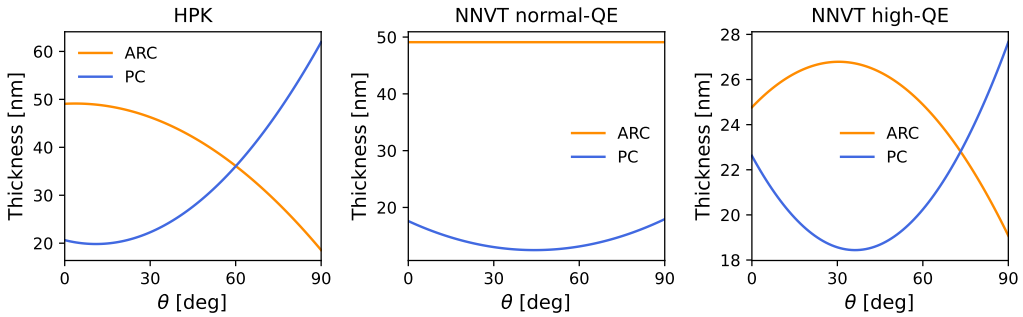


Figure 8. A typical example of the thickness curve of the PC and ARC as a function of zenith angles for HPK PMT (left), NNVT normal-QE PMT (middle), and NNVT high-QE PMT (right).

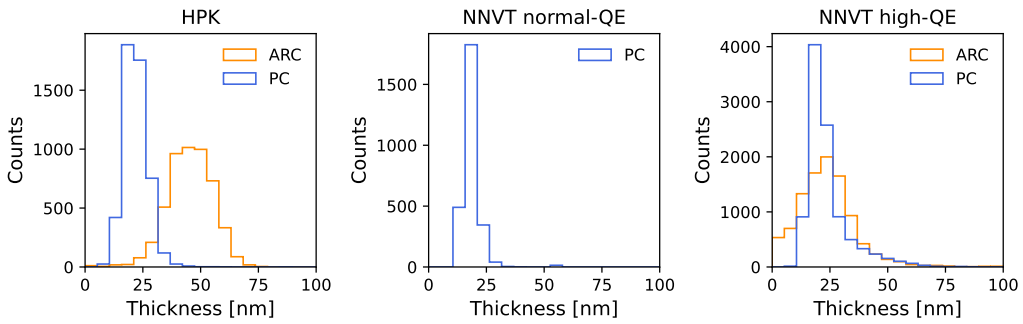


Figure 9. The thickness distributions of the PC and ARC at 0° for all HPK PMTs (left), NNVT normal-QE PMTs (middle), and NNVT high-QE PMTs (right).

us to determine the contributions from the various positions on the PC to PDE, taking into account the PC and ARC non-uniformity. From the simulation, both a and β can be derived for seven reference positions. Applying eq. (2.2), CE at these reference positions can be calculated for each PMT by solving the system of equations with the PDE data at each point.

Figure 10 presents the average CE over all PMTs of the same type, illustrating CE decreases with the increasing zenith angle. It is noted that some CE values are larger than one, which is a consequence of ignoring the variations of the escape factor among PMTs. In this work, it presents challenges when decomposing the F-factor into the escape factor and CE due to the lack of variation data of the escape factor among PMTs. Consequently, the assumption that the escape factor spectrum remains unchanged for each type of PMT introduces the bias in CE.

4.3 Spectral response of optical properties

The refractive index and extinction coefficient were measured for the PC and ARC of each type of PMT in [20] within the wavelength range of 390 nm to 500 nm. In this study, the dispersion relation is utilized to extend the refractive index of the ARC, covering the wavelength range of interest for JUNO from 300 nm to 700 nm:

$$n^2 - 1 = \frac{p_0 \lambda^2}{\lambda^2 - p_1} \tag{4.3}$$

2026 JINST 21 T06002

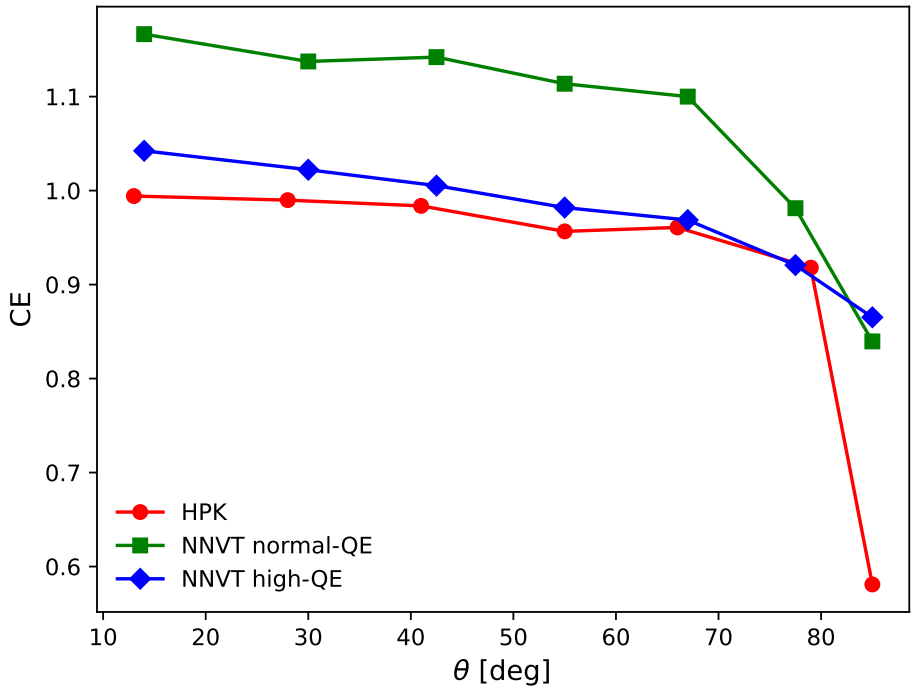


Figure 10. The average CE as a function of the zenith angle for HPK PMTs (red), NNVT normal-QE PMTs (green), and NNVT high-QE PMTs (blue).

where p_0 and p_1 are determined by fitting the measured refractive index of the ARC between 390 nm and 500 nm. The results of the refractive index of the ARC for three types of PMTs are shown in figure 11(a).

For the PC, the refractive index and extinction coefficient in the wavelength range of 300 nm to 390 nm and 500 nm to 700 nm are calculated with the permittivity (ϵ) of the bialkali PC reported in [23] with the following formula:

$$\epsilon = \epsilon' + i\epsilon'' = n^2 - k^2 + i2nk \tag{4.4}$$

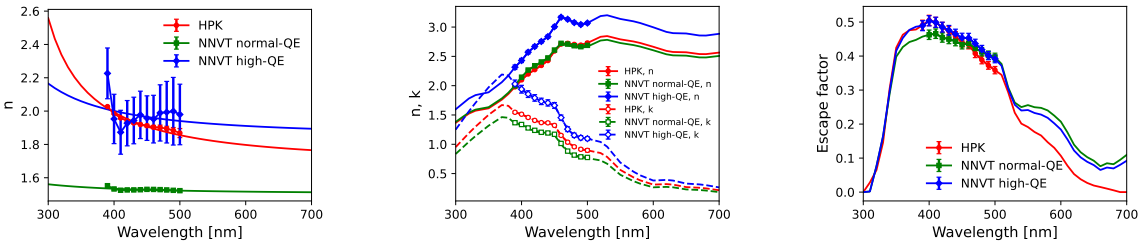
The calculated values in these two ranges are then normalized to the measured values at 390 nm and 500 nm as found in [20]. Figure 11(b) illustrates the results of the refractive index (solid lines) and extinction coefficient (dashed lines) of the PC across the full wavelength ranges for HPK PMT (red), NNVT normal-QE PMT (green), and NNVT high-QE PMT (blue).

The escape factor in the ranges of 300 nm to 390 nm and 500 nm to 700 nm is computed based on the measured QE spectra in [21] and respective absorption spectra, which is calculated with the aforementioned extended refractive index and extinction coefficient as well as the thickness values in [20] for both the PC and ARC, and then the escape factors are normalized to align with the measured curve reported in [20]. The results of the escape factor are shown in figure 11(c) for three types of PMTs.

4.4 Comparison of the average reflectance and PDE

To evaluate the potential impacts of the comprehensive PMT optical model on the JUNO detector energy response, we compare the average reflectance and PDE derived from the comprehensive model

2026 JINST 21 T06002



(a) Refractive index of ARC

(b) Refractive index and extinction coefficient of PC

(c) Escape factor

Figure 11. (a) The refractive index of the ARC as a function of the wavelength for HPK PMT (red), NNVT normal-QE PMT (green), and NNVT high-QE PMT (blue). (b) The refractive index (solid lines) and extinction coefficient (dashed lines) of the PC as a function of the wavelength for HPK PMT (red), NNVT normal-QE PMT (green), and NNVT high-QE PMT (blue). (c) The escape factor as a function of the wavelength for HPK PMT (red), NNVT normal-QE PMT (green), and NNVT high-QE PMT (blue).

to those obtained utilizing the simplified PMT optical model, where all PMTs of the same type are assumed to share the identical optical properties for the PC and ARC as described in [20].

Figure 12 illustrates the comparison results for the average reflectance (top) and PDE (bottom), which are weighted by the surface areas and averaged over all PMTs of the same type at 420 nm in water, as a function of the AOI, for HPK PMTs (left), NNVT normal-QE PMTs (middle), and NNVT high-QE PMTs (right). The blue solid lines represent the results from the non-uniform PC and ARC, while the orange dashed lines correspond to the simplified model. The green solid lines in the lower panels show the ratio of the results from two models. Notably, the comprehensive model predicts an increase in the reflectance for HPK PMTs, but a decrease of approximately 30% and 40% in the average reflectance for NNVT normal-QE and NNVT high-QE PMTs, respectively. The comprehensive model has less than a 2% effect on the average PDE in regions of the small AOI for all three PMT types, but a 5% to 10% impact on PDE at the large AOI. It is important to note that the PDE values presented here do not include the contributions from the transmitted photons, which are event-dependent and can be accounted for through simulation.

This comprehensive PMT optical model has been integrated into the JUNO simulation program, and a more detailed analysis of its effects on energy responses will be conducted. In addition, the outcomes derived from the comprehensive model will be compared with experimental JUNO data, and the model parameters may be further refined to improve alignment with actual data.

5 Conclusion

A precise PMT optical model is essential for improving the accuracy of the energy response of the JUNO detector, thereby enhancing the sensitivity and precision of JUNO physics outputs. In this study, we developed a comprehensive PMT optical model based on the previous research, aiming at extracting some basic optical parameters of PMTs and then precisely simulating the non-uniformity of PDE across the PMT surface and variations in PDE among different PMTs. The reflectance data collected from 669 PMTs in this work as well as the PDE data gathered from both the container system and scanning station system were utilized to constrain the thickness map of the PC and ARC for three types of 20-inch PMTs in JUNO: HPK PMTs, NNVT normal-QE PMTs, and NNVT high-QE PMTs.

2026 JINST 21 T06002

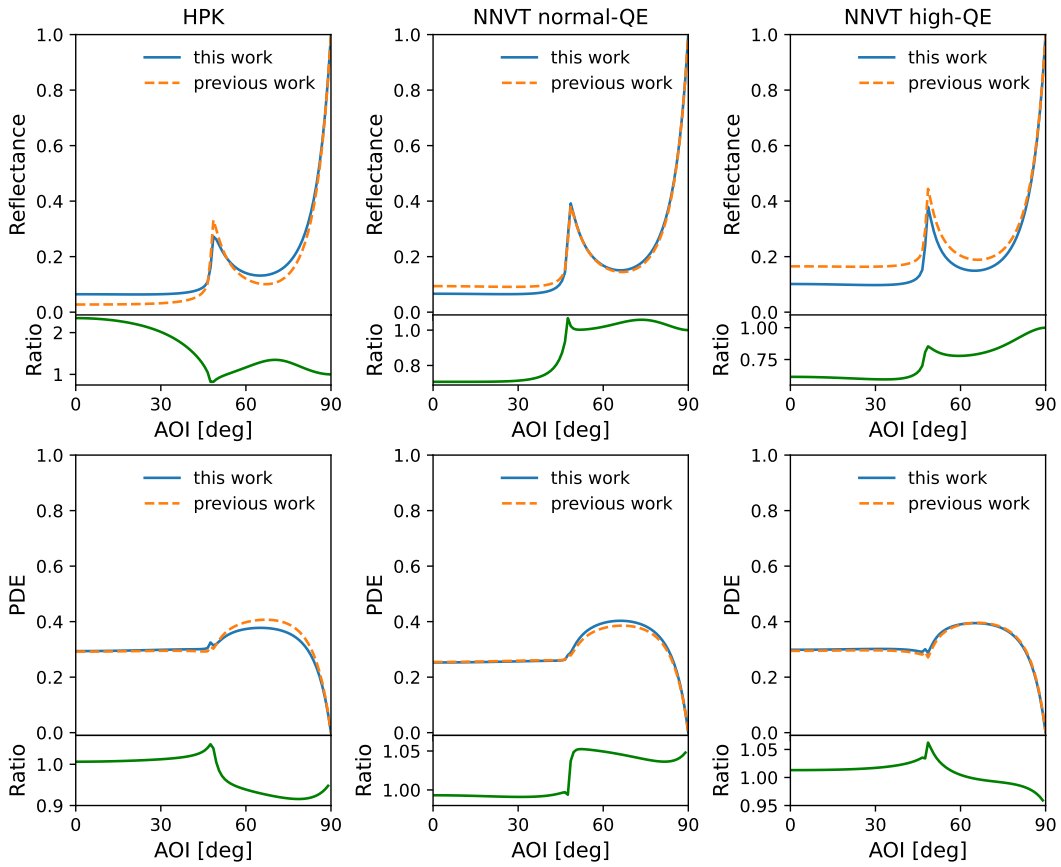


Figure 12. The average reflectance (top) and PDE without the contributions from the transmitted photons (bottom) as a function of the AOI for HPK PMTs (left), NNVT normal-QE PMTs (middle) and NNVT high-QE PMTs (right). The blue solid lines represent the results from the non-uniform ARC and PC, while the orange dashed lines indicate the results from the uniform ARC and PC, and the green solid lines show their ratio.

By performing a joint fit of both the reflectance and PDE data, we constructed the thickness map of the PC and ARC for each PMT. Taking into account the optical processes within PMTs by simulation, CE was determined as a function of the zenith angle by decomposing the PDE data. The refractive index and extinction coefficient of the PC and ARC, as well as the escape factor, were estimated over an extended wavelength range from 300 nm to 700 nm, covering the entire range of interest for JUNO.

Utilizing the new parameters for each PMT, we calculated the average reflectance and PDE, and compared these results with those from the simplified PMT optical model. The results show that PDE undergoes changes at the level of a few percent, and the reflectance exhibits significant changes of more than 30%. The comprehensive model has been incorporated into the JUNO simulation program, and its effects on the detector energy response will be thoroughly evaluated. Furthermore, additional refinements to the model have been ongoing since JUNO started physics data taking.

Acknowledgments

We gratefully acknowledge support from the National Natural Science Foundation of China (NSFC) under grant No. 12375196.

2026 JINST 21 T06002

References

[1] Borexino collaboration, *Science and technology of BOREXINO: A real time detector for low-energy solar neutrinos*, *Astropart. Phys.* **16** (2002) 205 [hep-ex/0012030].

[2] Borexino collaboration, *The Borexino detector at the Laboratori Nazionali del Gran Sasso*, *Nucl. Instrum. Meth. A* **600** (2009) 568 [arXiv:0806.2400].

[3] Daya Bay collaboration, *A precision measurement of the neutrino mixing angle θ_{13} using reactor antineutrinos at Daya-Bay*, hep-ex/0701029.

[4] Daya Bay collaboration, *Observation of electron-antineutrino disappearance at Daya Bay*, *Phys. Rev. Lett.* **108** (2012) 171803 [arXiv:1203.1669].

[5] KamLAND collaboration, *KamLAND: A reactor neutrino experiment testing the solar neutrino anomaly*, *Nucl. Phys. B Proc. Suppl.* **91** (2001) 99.

[6] KamLAND collaboration, *First results from KamLAND: Evidence for reactor anti-neutrino disappearance*, *Phys. Rev. Lett.* **90** (2003) 021802 [hep-ex/0212021].

[7] F. Suekane et al., *An overview of the kamland 1-kiloton liquid scintillator*, in the proceedings of the *KEK — RCNP International School and Miniworkshop for Scintillating Crystals and their Applications in Particle and Nuclear Physics*, Tsukuba, Japan, November 17–18 (2003) [physics/0404071].

[8] RENO collaboration, *RENO: An Experiment for Neutrino Oscillation Parameter θ_{13} Using Reactor Neutrinos at Yonggwang*, arXiv:1003.1391.

[9] RENO collaboration, *Observation of Reactor Electron Antineutrino Disappearance in the RENO Experiment*, *Phys. Rev. Lett.* **108** (2012) 191802 [arXiv:1204.0626].

[10] Hamamatsu Photonics K.K., *R12860 datasheet*, https://www.hamamatsu.com/jp/en/product/optical-sensors/pmt/pmt_tube-alone/head-on-type/R12860.html.

[11] Y. Wang et al., *A new design of large area MCP-PMT for the next generation neutrino experiment*, *Nucl. Instrum. Meth. A* **695** (2012) 113.

[12] JUNO collaboration, *JUNO Conceptual Design Report*, arXiv:1508.07166.

[13] JUNO collaboration, *Neutrino Physics with JUNO*, *J. Phys. G* **43** (2016) 030401 [arXiv:1507.05613].

[14] JUNO collaboration, *JUNO physics and detector*, *Prog. Part. Nucl. Phys.* **123** (2022) 103927 [arXiv:2104.02565].

[15] JUNO collaboration, *First measurement of reactor neutrino oscillations at JUNO*, arXiv:2511.14593.

[16] JUNO collaboration, *Initial performance results of the JUNO detector*, *Chin. Phys. C* **50** (2026) 043001 [arXiv:2511.14590].

[17] JUNO collaboration, *Mass testing and characterization of 20-inch PMTs for JUNO*, *Eur. Phys. J. C* **82** (2022) 1168 [arXiv:2205.08629].

[18] JUNO collaboration, *Potential to identify neutrino mass ordering with reactor antineutrinos at JUNO*, *Chin. Phys. C* **49** (2025) 033104 [arXiv:2405.18008].

[19] W.E. Spicer, *Photoemissive, Photoconductive, and Optical Absorption Studies of Alkali-Antimony Compounds*, *Phys. Rev.* **112** (1958) 114.

[20] Y. Wang, G. Cao, L. Wen and Y. Wang, *A new optical model for photomultiplier tubes*, *Eur. Phys. J. C* **82** (2022) 329 [arXiv:2204.02703].

[21] JUNO collaboration, *Prediction of Energy Resolution in the JUNO Experiment*, *Chin. Phys. C* **49** (2025) 013003 [arXiv:2405.17860].

[22] GEANT4 collaboration, *GEANT4 — A Simulation Toolkit*, *Nucl. Instrum. Meth. A* **506** (2003) 250.

[23] S.W. Harmer, R. Downey, Y. Wang and P.D. Townsend, *Variation in optical constants between photocathodes*, *Nucl. Instrum. Meth. A* **564** (2006) 439.

2026 JINST 21 T06002